10-18-2004

Analysis of Chaos-Induced Pulse Trains in the Ionization of Hydrogen

K. A. Mitchell

J. P. Handley

B. Tighe

A. Flower

J. B. Delos

Analysis of chaos-induced pulse trains in the ionization of hydrogen

K. A. Mitchell,* J. P. Handley, B. Tighe, A. Flower, and J. B. Delos†
Department of Physics, College of William and Mary, Williamsburg, Virginia 23187-8795, USA
(Received 3 April 2004; published 18 October 2004)

We examine excitation (by a short laser pulse) of a hydrogen atom in parallel electric and magnetic fields, from an initial tightly bound state to a state above the classical ionization threshold. We predict that the atom ionizes by emitting a train of electron pulses. This prediction is based on the classical dynamics of electron escape. In particular, the pulse train is due to classical chaos, which occurs for nonvanishing magnetic field. We connect the structure of the pulse train to fractal structure in the escape dynamics, and discuss several issues of experimental interest, with a particular emphasis on understanding the resolution of individual pulses. A brief account of this work appeared previously as a Letter [Phys. Rev. Lett. **92**, 073001 (2004)].

DOI: 10.1103/PhysRevA.70.043407 PACS number(s): 32.80.Rm, 32.80.Fb, 05.45.Ac, 05.45.Df

I. INTRODUCTION

Our work is motivated by the experiments of Lankhuijzen and Noordam [1], in which rubidium atoms in a constant applied electric field were excited from the ground state to an energy above the classical saddle by a short (few picosecond) laser pulse. The resulting electron flux striking a detector was then measured as a function of time. This ionization signal revealed a train of electron pulses, rather than an exponential decay. This observation can be qualitatively explained by the following semiclassical analysis [2]. Photoabsorption promotes the valence electron from a low-energy bound state into an outgoing wave, which can be modeled semiclassically as an ensemble of trajectories propagating away from the atomic core in all directions and with a narrow range of energies. Some trajectories head directly downhill, and are accelerated by the external field toward a detector, creating an initial prompt pulse of electrons. Other trajectories initially head uphill, are turned around by the field, and return to the core where they scatter in all directions. Some of these scattered trajectories head downhill, creating a second pulse of electrons. Subsequent rescattering events create additional pulses. Similar results have also been obtained in quantum computations [2].

Here, we predict that a hydrogen atom, placed in combined electric and magnetic fields, can also ionize through emission of an electron pulse train. (This prediction originally occurred as a Letter [3].) Though these pulse trains bear a certain similarity to those found experimentally for rubidium, the mechanism for pulse creation is fundamentally different. Pulses are not created through core scattering (since there are no core electrons). Rather, the pulses are a result of classical chaos, which occurs for nonvanishing magnetic field. This can be outlined as follows. Due to the chaotic dynamics, the behavior of a trajectory moving away from the nucleus depends intricately upon its initial outgoing angle θ [4]. Nevertheless, over certain intervals of θ (called escape segments), all trajectories have similar qualitative behavior, and most strike the detector within a short interval of time. Thus the family of trajectories within each escape segment gives rise to a single electron pulse.

More formally, we identify the escape segments by first reducing the electron dynamics from a Hamiltonian flow to an area-preserving map on a two-dimensional phase space. This map possesses a prominent fixed point, related to a periodic orbit of the full electron dynamics. The stable and unstable manifolds of this fixed point (which are curves in the plane) intersect to form what is called a homoclinic tangle. Homoclinic tangles are a basic mechanism for chaotic transport and escape, and the intricate manner in which the unstable manifold intersects the initial ensemble of trajectories (which itself is well approximated by a line in the plane) defines the escape segments.

The escape segments exhibit fractal structure-within-structure as well as a certain self-similarity, which we call "epistrophic self-similarity." This fractal structure is reflected in the structure of the pulse train. Here, we concentrate on the early time behavior, embodied in the first several pulses. The pulse train becomes more and more complicated as time progresses.

Our theoretical analysis is intended to stimulate experimental efforts to observe chaos-induced pulse trains in hydrogen, or related systems. Such observations would not only elucidate a fundamental ionization mechanism, but would also provide a convenient laboratory tool for studying chaotic transport and escape.

Our paper is summarized as follows. Section II lays the foundation for the theory of the ionization process. In particular, Sec. II B explains how the initial outgoing wave packet is modeled by a classical ensemble of trajectories moving away from the nucleus. The classical propagation of this ensemble yields an electron pulse train striking the detector, first illustrated in Sec. II C. Section II D connects the pulse train to the "fractal" escape-time plot—the time it takes a trajectory to strike the detector plotted as a function of its initial outgoing angle θ.

Section III examines the classical dynamics of ionizing trajectories. In particular, after transforming to parabolic coordinates (Sec. III A) and identifying a particularly important

*Permanent address: School of Natural Sciences, University of California, Merced, CA 95344, USA. Electronic address: kmitchell@ucmerced.edu
†Electronic address: jbdelo@wm.edu

periodic orbit (Sec. III B), we introduce a two-dimensional surface of section in phase space, which allows the dynamics to be reduced to a discrete-"time" Poincaré return map (Sec. III C), Section III D discusses the escape mechanism associated with the homoclinic tangle of this map.

Section IV discusses regular features of the fractal structure, with a focus on "epistrophes" —regular sequences of escape segments that occur on all scales throughout the escape-time plot. Section IV B describes the relevance of epistrophes to the pulse train. Section IV C illustrates how changes in the structure of the tangle are reflected in the pulse train.

Section V analyzes the averaging of the pulse train over a distribution of energies Δ_E and launch times Δ_t. Specifically, we derive an optimal laser pulse length (Sec. V B); we illustrate the advantage of exciting to higher N states (Sec. V C); and we examine the benefits of chirped laser pulses (Sec. V E). In Sec. V F, we consider different initial angular states, e.g., due to different laser excitation schemes.

Section VI presents our conclusions. Finally, Appendix A gives a perturbative analysis of the dynamics in the vicinity of the prominent periodic orbit, and Appendix B considers the (minimal) dependence of the pulse train on the detector position.

II. OVERVIEW OF THE IONIZATION PROCESS

The ionization process is summarized as follows. The hydrogen atom is placed in parallel external electric and magnetic fields, with the electron in a low-energy eigenstate; the applied fields are not strong enough to significantly alter this state. Next, a short laser pulse strikes the atom, promoting a fraction of the initial electron state to an energy above the classical ionization threshold, forming a radial wave packet. That is, just as a pebble dropped into a pond produces a circular outgoing ripple, photoexcitation of the atom by a short laser pulse produces a spherical outgoing wave packet, which propagates away from the atom in all directions. The wave packet evolves in the Coulomb field of the proton plus the applied electric and magnetic fields. Over the course of time, some of the wave packet slips over the classical barrier, is drawn downhill by the applied electric field, and strikes the detector, which measures the ionization rate (defined as the rate of electrons striking the detector) as a function of time.

A. Hamiltonian and scaled variables

The Hamiltonian H of the electron in Coulomb plus applied parallel electric and magnetic fields is given in cylindrical coordinates (ρ,z) and atomic units $(e=\hbar=m_e=1)$ by

$$H(\rho,z,p_\rho,p_z)=\frac{1}{2}(p_\rho^2+p_z^2)+V(\rho,z)=E, \tag{1a}$$

$$V(\rho,z)=-\frac{1}{\sqrt{\rho^2+z^2}}+z+\frac{1}{8}B^2\rho^2, \tag{1b}$$

where the linear term in B is eliminated by working in a frame rotating about the z axis with frequency $\omega=B/2$; for simplicity the z component of angular momentum $\hat{\mathbf{z}}\cdot(\mathbf{r}\times\mathbf{p})$ is set to zero. As is common [e.g., Refs. [5(b),6]], Eq. (1) is expressed in scaled variables (ρ,z,p_ρ,p_z) that are related to the original unscaled variables $(\hat{\rho},\hat{z},\hat{p}_\rho,\hat{p}_z)$ by $(\rho,z)=(\hat{\rho}\hat{F}^{1/2},\hat{z}\hat{F}^{1/2})$ and $(p_\rho,p_z)=(\hat{p}_\rho\hat{F}^{-1/4},\hat{p}_z\hat{F}^{-1/4})$, where $\hat{F}$ is the applied electric-field strength (in atomic units). The scaled energy is $E=\hat{E}\hat{F}^{-1/2}$ and the scaled magnetic-field strength is $B=\hat{B}\hat{F}^{-3/4}$, where $\hat{E}$ and $\hat{B}$ are the corresponding physical values (in atomic units). Similarly, the scaled time is $t=\hat{t}\hat{F}^{3/4}$.

Applying the preceding scalings to the quantum momentum operators, $\hat{p}_j=-i\hbar\,\partial/\partial\hat{q}_j$ implies $p_j=-i\hbar_s\,\partial/\partial q_j$, where $\hbar_s=\hbar\hat{F}^{1/4}=\hbar(\hat{E}/E)^{1/2}$ is a scaled version of the Planck constant. In atomic units $(\hbar=1)$,

$$\hbar_s=\frac{1}{N\sqrt{2|E|}}, \tag{2}$$

where $N=(2|\hat{E}|)^{-1/2}$ is the ersatz principal quantum number. Equation (2) confirms one's intuition that by exciting the atom to higher energies, the effective value of Planck's constant is lowered, and the system is more "classical."

B. The initial outgoing wave packet

The laser field contributes an additional term to the Hamiltonian,

$$H_L(t)=F_L D g(t), \tag{3}$$

where F_L is the peak electric-field strength (in scaled units), $D=\mathbf{r}\cdot\boldsymbol{\epsilon}$ is the dipole operator, with laser polarization $\boldsymbol{\varepsilon}$ and electron position $\mathbf{r}$, and $g(t)$ is the time dependence. We include only the absorption term of the laser field, for which we assume $g(t)=g_{\rm env}(t)\exp(-i\omega_L t)$, with ω_L the central laser frequency and $g_{\rm env}(t)$ a slowly varying envelope centered about $t=0$ and having a maximum amplitude of 1. We typically use a Gaussian $g_{\rm env}(t)=\exp[-t^2/(4\Delta_t^2)]$, where Δ_t is the standard deviation of the *intensity* of the laser pulse. In Eq. (3) and the remainder of Sec. II B, we work in an inertial frame.

Using first-order time-dependent quantum perturbation theory, the initial Coulomb eigenstate $|\psi_i\rangle$ generates the excited time-dependent state $|\Psi_x(t)\rangle$ according to

$$\begin{aligned}(i\hbar_s\,\partial/\partial t-H)|\Psi_x(t)\rangle&=H_L(t)\exp(-iE_i t/\hbar_s)|\psi_i\rangle\\&=F_L g_{\rm env}(t)\exp(-iE_c t/\hbar_s)D|\psi_i\rangle=|S(t)\rangle,\end{aligned} \tag{4}$$

where E_i is the energy of $|\psi_i\rangle$ and $E_c=E_i+\hbar_s\omega_L$ is the central energy of the excited state $|\Psi_x(t)\rangle$. The inhomogeneous term $|S(t)\rangle$ acts as a source for $|\Psi_x(t)\rangle$, yielding

$$\Psi_x(\mathbf{r},t)=\int_{-\infty}^{\infty}d\mathbf{r}'dt'K(\mathbf{r},t;\mathbf{r}',t')S(\mathbf{r}',t'), \tag{5}$$

where $K(\mathbf{r},t;\mathbf{r}',t')$ is the propagator for H.

References [5–8] discuss excitation by a steady-state laser, i.e., $g_{\rm env}=1$, to a definite energy close to the zero-field ionization threshold (i.e., N is large). In this case, the compact source $|S\rangle$ generates an outgoing spherical Coulomb wave $\psi_{\rm out}(\boldsymbol{r})$ in the vicinity of the atom, where the external fields are not strong enough to be significant. At a sufficiently large radius, this wave is well approximated by the decomposition [Ref. [6], Eq. (2.12)]

$$\psi_{\rm out}(\boldsymbol{r}) = \frac{C}{r^{3/4}} \exp(i\sqrt{8r}/\hbar_s)\mathcal{Y}(\theta,\phi), \tag{6}$$

where $\mathcal{Y}(\theta,\phi)$ gives the angular distribution of the wave and C is a constant. The spherical angles θ and ϕ are defined relative to the positive z axis. The outgoing wave can be described semiclassically by an ensemble of classical trajectories moving radially away from the nucleus; these trajectories have a fixed energy E and are continuously emitted from the source for all times, with angular distribution $|\mathcal{Y}(\theta,\phi)|^2$. The subsequent evolution of these trajectories describes the steady-state quantum wave function.

The computation of $\mathcal{Y}$ in terms of the initial state $|\psi_i\rangle$ and the dipole operator D is discussed in Ref. [6], Appendix A3 and Ref. [5(b)], Sec. V B. See also [7]. Assuming the z component of the angular momentum is zero, as in Eq. (1), $\mathcal{Y}(\theta,\phi)$ reduces to $\mathcal{Y}(\theta)$.

For the pulsed laser considered here, the outgoing wave $\psi_{\rm out}(\boldsymbol{r})$ is primarily emitted over the time interval Δ_t determined by $g_{\rm env}(t)$. The energy of the wave is not sharp, but has a deviation Δ_E about the central energy E_c, satisfying the uncertainty relation $\Delta_E\Delta_t \geqslant \hbar_s/2$ (equality for a Gaussian pulse.) A sufficiently tight energy resolution ensures the validity of Eq. (6), meaning the (physical) time interval should be much longer than an atomic unit, or in scaled units $\Delta_t \gg 1/N^3$. Semiclassically, we then model the electron pulse by an ensemble of classical trajectories that have a range of launch times Δ_t and a range of energies Δ_E.

More formally, the initial distribution of trajectories in the energy-time plane is given by the Wigner function $W_f(E,t)$ of $f(t)=g_{\rm env}(t)\exp(-iE_ct/\hbar_s)$,

$$W_f(E,t) = \int_{-\infty}^{\infty} ds\; e^{isE/\hbar_s} f(t+s/2) f^*(t-s/2). \tag{7}$$

The Wigner function is the quantum analog of a classical phase-space density. For a Gaussian envelope $g_{\rm env}(t) = \exp[-t^2/(4\Delta_t^2)]$, the Wigner function of $f(t)$ is itself a Gaussian,

$$W_f(E,t) = Ae^{-t^2/(2\Delta_t^2)} e^{-(E-E_c)^2/(2\Delta_E^2)}, \tag{8}$$

with normalization $A=2\sqrt{2\pi}\Delta_t$ and $\Delta_E=\hbar_s/(2\Delta)_t$. The initial electron wave packet is modeled by a classical ensemble of trajectories beginning at the nucleus and propagating radially outward with a distribution of energies and launch times given by $W_f(E,t)$ and a distribution of launch angles θ given by $|\mathcal{Y}(\theta)|^2\sin\theta$. So long as $|\mathcal{Y}(\theta)|^2$ is independent of ϕ, this outgoing distribution is valid in either an inertial frame or the rotating frame of Eqs. (1).

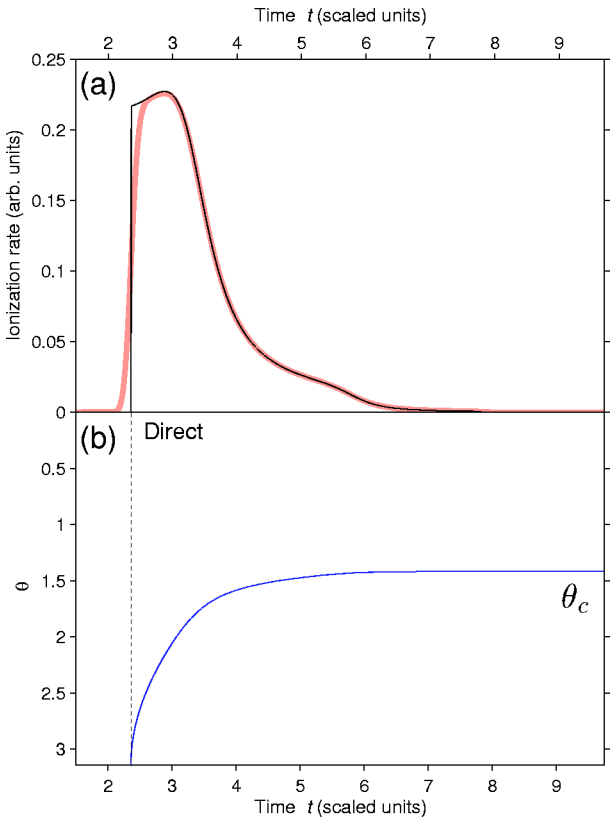

FIG. 1. (a) For hydrogen in an electric field only ($B=0$ and scaled energy $E=-1.3$), the electron flux (ionization rate) striking the detector (at $z=-4$) is plotted as a function of time after atomic excitation. The thin dark line models the outgoing electron wave packet by an ensemble of trajectories with precise energy and launch time. The thick shaded line uses an ensemble represented by a minimum uncertainty Gaussian wave packet with $\Delta_t=\Delta_E=0.062$. The central (physical) energy of the wave packet is $\hat{E}=-1/(2N^2)$ with $N=80$. This implies $\hat{F}=19$ V/cm and one scaled unit of time t equals 52 ps. (b) The time it takes a trajectory to strike the detector is plotted as a function of the initial launch angle θ.

Within semiclassical theory, the evolution of the initial wave packet is approximated by following the trajectories within the corresponding classical distribution. This approximation involves both evolving the classical density (the square root of the density yields the quantum amplitude) as well as determining the quantum phase (by computing the accumulated action). In this paper, we ignore the phase information (that is, we ignore interference) and concentrate on the classical density. For early times and for sufficiently high excitation (large N), this should yield a reasonable approximation to the intensity seen at the detector.

C. Numerical computation of the ionization rate

Figure 1(a) shows the ionization rate computed for zero magnetic field. The computation begins with an initial ensemble of radially outgoing trajectories as described in Sec. II B. These trajectories are integrated until they reach the detector, located at $z=-4$, or until some maximum cutoff

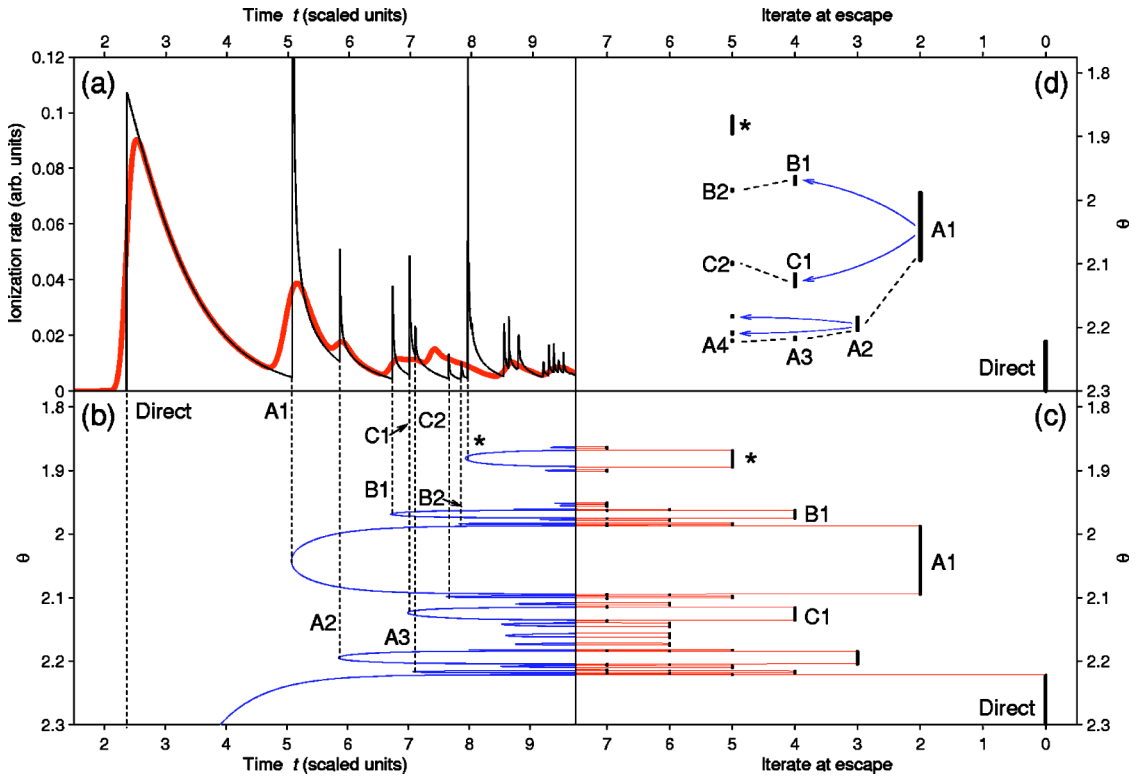

FIG. 2. The ionization rate for hydrogen in parallel fields, with $B=4.5$, $E=-1.3$, is plotted vs the time after atomic excitation. As in Fig. 1(a), the thin dark line uses an ensemble with precise energy and launch time, and the thick shaded line uses a Gaussian wave packet of the same form as in Fig. 1(a). In this case, $N=80$ yields a physical magnetic-field strength of $\hat{B}=0.49$ T. (b) The time it takes a trajectory to strike the detector is plotted as a function of the initial launch angle θ. The dashed lines connect icicles to their corresponding pulses in (a). The lowest icicle, having only its upper portion visible in Fig. 2(b), represents the direct trajectories. (c) The number of iterates of the Poincaré map required to escape the complex is plotted vs θ. Each escape segment corresponds to an icicle in (b). (d) The epistrophic structure of the first several escape segments is shown. The dashed lines connect segments within one epistrophe. The solid arrows show the creation of new epistrophes according to the Epistrophe Start Rule. The asterisk denotes a strophe segment which does not fit into the pattern of epistrophes.

time is attained.[1] The total number of trajectories striking the detector per unit time (the ionization rate) is then recorded as a function of time. The thin line in Fig. 1(a) is the unaveraged ionization rate, computed using a classical ensemble with a single fixed energy $E=-1.3$ and a precise launch time $t=0$. The thick line is the result using a Gaussian distribution (8) of energies and launch times, with $\Delta_t=\Delta_E=0.062$ and central energy $E_c=-1.3$. Both lines show a single pulse of electrons, with an exponentially decaying tail. The thick line is simply a smoothed version of the thin line, since the behavior of the trajectories does not vary significantly over Δ_E.

Figure 2(a) shows the ionization rate for nonzero magnetic field $B=4.5$; all other parameters are as in Fig. 1(a). The thin line in Fig. 2(a), for fixed energy $E=-1.3$ and launch time $t=0$, exhibits a train of pulses, in sharp contrast to the single pulse in Fig. 1(a). The thick line averages out this structure somewhat, but pulses are still discernible. As time increases, the pulses proliferate and overlap, merging to form a "lumpy" tail.

[1]The detector position $z=-4$ is unrealistically close to the atom. However, Appendix B shows that this makes little difference in our results.

In both Figs. 1(a) and 2(a), the angular distribution is an s wave, with $\mathcal{Y}=1$. This distribution is chosen for theoretical convenience, since it weights all directions evenly. In Sec. V F, we consider other distributions which may be more experimentally appropriate.

We focus first on understanding pulse trains generated by a fixed energy E and launch time $t=0$, i.e., the thin lines.

D. The escape-time plot

We examine first the case of no magnetic field. Figure 1(b) shows the time it takes a trajectory (with fixed $E=-1.3$ and $B=0$) to strike the detector as a function of its initial outgoing angle θ. The trajectory that heads directly downhill ($\theta=\pi$) reaches the detector first. As θ decreases, the initial velocity points further and further away from the downhill direction, and the trajectory takes longer and longer to strike the detector. Eventually a critical angle θ_c is reached, at which the trajectory takes an infinite time to escape. This trajectory is bound forever. All trajectories above the critical angle are also bound forever.

The thin ionization curve in Fig. 1(a) is equal to the slope $d\theta/dt$ of the escape-time plot in Fig. 1(b), weighted by the

initial angular distribution $|\mathcal{Y}(\theta)|^2 \sin\theta$. The pulse in Fig. 1(a) starts at the earliest escape time in Fig. 1(b) and then trails off to zero as θ approaches the critical angle and $d\theta/dt$ goes to zero.

We now turn on the magnetic field. Figure 2(b) shows the escape-time plot for $E=-1.3$, $B=4.5$, with the range of θ restricted to the transition region between direct trajectories that strike the detector quickly at large θ and trajectories that are bound for a long (possibly infinite) time at small θ. This transition is much more complicated than in Fig. 1(b). Rather than a single critical angle, there are many critical angles (in fact, an infinite number), with fractal behavior and structure on all scales [9]. Following Ref. [10], we use the term "icicle" for a smooth region of the plot located between two critical angles.

As in Fig. 1, the slope $d\theta/dt$ in Fig. 2(b), together with the weighting $|\mathcal{Y}(\theta)|^2 \sin\theta$, yields the thin ionization curve in Fig. 2(a). Each icicle, therefore, contributes one pulse to the train. The pulse begins at the tip, or earliest time, of an icicle, where $d\theta/dt$ is infinite. The initial pulse height is therefore also infinite, so long as the weight factor $|\mathcal{Y}(\theta)|^2 \sin\theta$ does not vanish. (The height of the direct pulse is finite since this factor vanishes sufficiently rapidly at $\theta=\pi$.) The area underneath a pulse is finite, regardless of its initial height [i.e., the singularity is integrable, being proportional to $(t-t_0)^{-1/2}$], and equals $|\mathcal{Y}(\theta)|^2 \sin\theta$ integrated across the θ range of the icicle. A pulse eventually exhibits exponential decay as one moves out along an edge of the icicle (assuming the edge does not coincide with a zero of the weight factor.) Parts (c) and (d) of Fig. 2 will be discussed later, in Sec. IV A.

In conclusion, to understand the structure of the electron pulse train, we must explore the structure of the escape-time plot. This, in turn, requires a detailed understanding of the classical escape dynamics.

III. CLASSICAL ESCAPE DYNAMICS

A. Transformation to parabolic coordinates

Following standard practice [e.g., Refs. [5(b),5(c)]], we define parabolic coordinates (u,v) and their conjugate momenta (p_u,p_v) by

$$u = \pm\sqrt{r+z}, \quad v = \pm\sqrt{r-z}, \tag{9}$$

$$p_u = vp_\rho + up_z, \quad p_v = up_\rho - vp_z, \tag{10}$$

where $r=\sqrt{\rho^2+z^2}=(u^2+v^2)/2$. We allow u and v to take both positive and negative values $(-\infty<u,v<\infty)$ corresponding to a fourfold covering of the cylindrical coordinates $(\rho\geqslant 0, -\infty<z<\infty)$. Equations (9) and (10) have the following inverse transformations:

$$\rho = uv, \quad z = \frac{1}{2}(u^2-v^2), \tag{11}$$

$$p_\rho = \frac{vp_u+up_v}{u^2+v^2}, \quad p_z = \frac{up_u-vp_v}{u^2+v^2}. \tag{12}$$

We introduce an effective Hamiltonian $h=2r(H-E)$, which equals

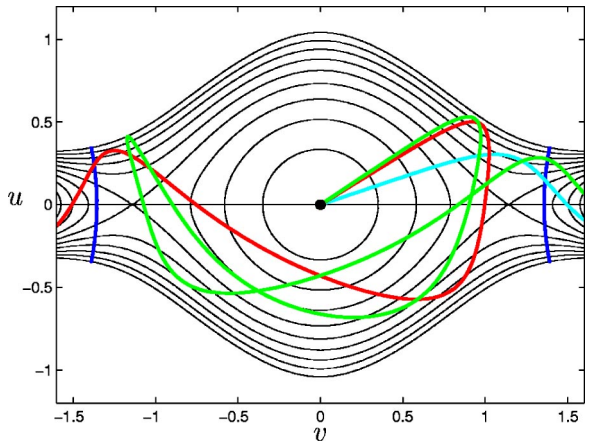

FIG. 3. A contour plot of the effective potential V_{uv} ($B=4.5$, $E=-1.3$) is shown with unstable periodic orbits (vertical curves) placed symmetrically near the left and right saddle points. Three ionizing trajectories are also shown.

$$h(u,v,p_u,p_v) = \frac{1}{2}(p_u^2+p_v^2) + V_{uv}(u,v) - 2, \tag{13a}$$

$$V_{uv}(u,v) = -E(u^2+v^2) + \frac{1}{8}B^2(u^4v^2+u^2v^4) + \frac{1}{2}(u^4-v^4). \tag{13b}$$

Setting $h=0$, this Hamiltonian generates the same trajectories as setting $H=E$, although parameterized by a new timelike variable s, defined by $ds/dt=1/(2r)$. Note that E appears as a parameter in the Hamiltonian h.

In Eq. (13b), B^2 acts as a coupling constant between the u and v motions. When $B=0$, the Hamiltonian is separable, and there is no chaos. When $B\neq 0$, mixing between the u and v motions produces chaos responsible for the pulse train.

The effective potential V_{uv}, plotted in Fig. 3, contains a smooth well about the nucleus $(u=v=0)$. The elimination of the Coulomb singularity makes the numerical propagation of trajectories near the nucleus more tractable. Several ionizing trajectories are also drawn in Fig. 3. They begin at the nucleus, undergo some oscillations within the potential well, and then eventually pass over the saddle region and escape through either the left or right exit channel. The left and right exit channels are physically equivalent since $+(u,v)$ and $-(u,v)$ correspond to the same physical position. [See Eq. (11).] Figure 3 is analogous to Fig. 2 of Ref. [3], which is presented in the physical ρz coordinates.

B. An important periodic orbit

Figure 3 shows two symmetrically placed periodic orbits near $v=\pm 1.3$. Any escaping trajectory must cross the curve formed by one of these orbits. This curve is called a *periodic orbit dividing surface*, or PODS, in molecular reaction theory [11]. It acts as a kind of gatekeeper to escape. Once a trajectory has crossed over the curve into the exit channel, it cannot return.

The two periodic orbits in uv space reduce to a single physical orbit in ρz space. The period $T_{\rm po}$ of this orbit plays

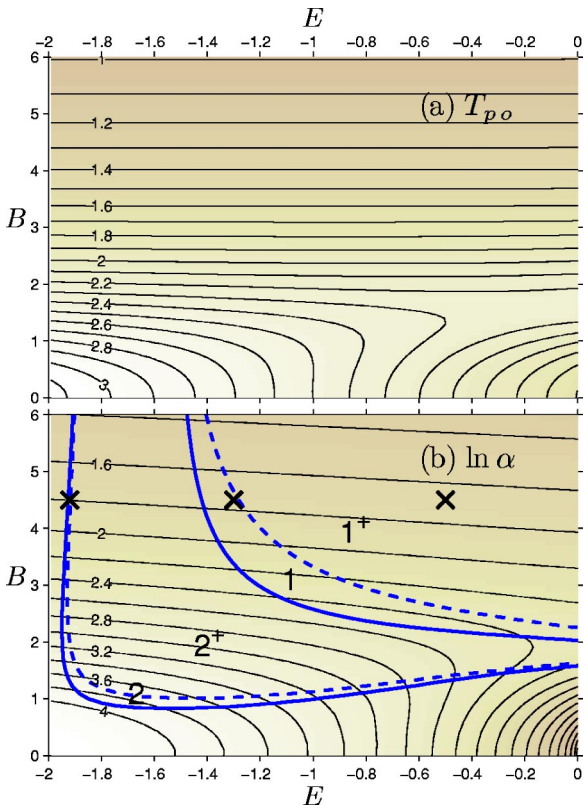

FIG. 4. Contour plots of (a) the time $T_{\rm po}$ for the periodic orbit to leave and return to the u axis and (b) the Liapunov exponent ln α of the periodic orbit. For (b), $D=1$ in regions 1 and 1^+ and $D=2$ in regions 2 and 2^+. The dashed lines separate regions with and without overshoot (see Sec. IV C). The three X's mark $B=4.5$ with $E=-1.92,-1.3,-0.5$, which are used for numerical computations in this paper.

a critical role in our analysis. Here, $T_{\rm po}$ is the time it takes the orbit to travel from $\rho=0$ back to $\rho=0$, maintaining $\rho>0$ (equivalently $u>0$), i.e., $T_{\rm po}$ is half the period of the orbit in Fig. 3. Figure 4(a) plots $T_{\rm po}$ computed numerically as a function of E and B. For $B\gtrsim 2$, the period is approximately (see Appendix A)

$$T_{\rm po} \approx \frac{2\pi}{\sqrt{B^2+4}} \tag{14}$$

with frequency $\omega_{\rm po}\approx\sqrt{B^2+4}$. This approximation is independent of E and falls to zero as B goes to infinity, consistent with Fig. 4(a). Furthermore, in the large B limit, $T_{\rm po}$ reduces to the cyclotron period $T_{\rm cycl}=2\pi/B$ (as it must). For $E=-1.3$ and $B=4.5$, direct numerical computation yields $T_{\rm po}=1.2752$, whereas Eq. (14) yields the close approximation $T_{\rm po}=1.2759$. Part (b) of Fig. 4 will be discussed later, in Sec. III D.

C. Surface of section and Poincaré map

We define a two-dimensional Poincaré surface of section in the four-dimensional (u,v,p_u,p_v) phase space by the constraints $u=h=0$. A point on this surface is specified, up to the sign of p_u, by its coordinates (v,p_v). The Poincaré return

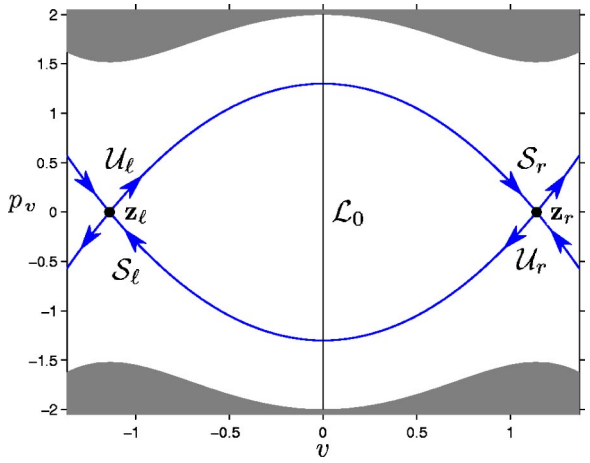

FIG. 5. The surface-of-section plot for $B=0$, $E=-1.3$ shows left and right fixed points, $\mathbf{z}_\ell$ and $\mathbf{z}_r$, whose stable mainfolds, $\mathcal{S}_\ell$ and $\mathcal{S}_r$, coincide with their unstable manifolds, $\mathcal{U}_r$ and $\mathcal{U}_\ell$. The initial electron trajectories populate the vertical line $\mathcal{L}_0$. The shaded regions are energetically forbidden.

map, a discrete-time map on the surface of section, is defined as follows. An initial point on the surface evolves under the Hamiltonian (13). The trajectory initially moves away from the v axis in the uv plane, but is ultimately turned around by the potential $V(u,v)$, subsequently returning to the v axis and intersecting the surface of section. This new intersection is defined to be the image of the initial point under the Poincaré map. We view the Poincaré map as a map from the initial coordinates (v,p_v) to the final coordinates (v',p_v'); this interpretation is possible because it does not depend on the sign of p_u.

We examine the Poincaré map first for zero magnetic field. Figure 5 is the surface-of-section plot for $B=0$, $E=-1.3$. Within this plot are left and right fixed points z_l and z_r, located where the two periodic orbits in Fig. 3 puncture the surface of section. Each of these fixed points is unstable, and the attached curves are its stable and unstable manifolds (that is, the sets of points that converge to the fixed point under forward and backward iterates, respectively.) In this case, a branch $\mathcal{U}_\ell$ of the left unstable manifold exactly coincides with a branch $\mathcal{S}_r$ of the right stable manifold, and vice versa. The other four branches go to infinity and do not intersect.

Notice that the surface-of-section plot is invariant under $(v,p_v)\mapsto-(v,p_v)$. In fact, the points (v,p_v) and $-(v,p_v)$ on the surface $u=0$ are physically identical, as seen from Eqs. (11) and (12).

All trajectories that are launched from the nucleus at the precise time $t=0$ and with a precise energy start at $u=v=0$ with $h=0$ and with the parameter E in Eq. (13) fixed. Thus, the initial ensemble populates the line $\mathcal{L}_0$, which is that segment of the p_v axis within the energetically allowed region of the surface of section. This line is parametrized by the initial outgoing angle θ according to $p_v=2\sin\theta/2$, as derived from Eqs. (9) and (10) and the fact that $p_u^2+p_v^2=4$ at $u=v=0$.

The line of initial conditions $\mathcal{L}_0$ intersects the stable/unstable manifolds at two points, corresponding to the single (physical) critical angle θ_c in Fig. 1(b). Within the eye-

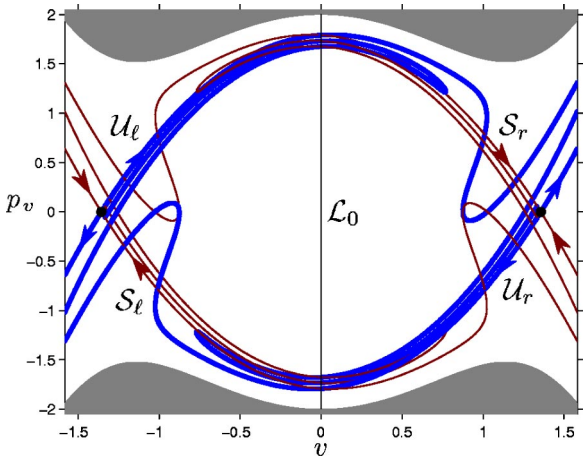

FIG. 6. The surface-of-section plot for $B=4.5$, $E=-1.3$ shows that the right stable manifold $\mathcal{S}_r$ (thin solid curve) and left unstable manifold $\mathcal{U}_\ell$ (thick dashed curve) no longer coincide. The same is true of S_ℓ and $\mathcal{U}_r$.

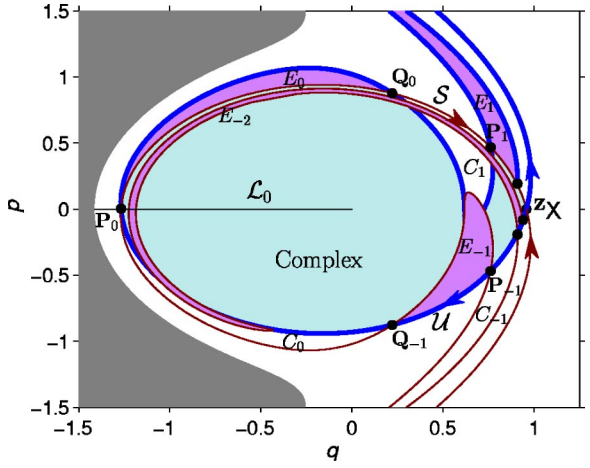

FIG. 7. The surface-of-section plot for $B=4.5$, $E=-1.3$ in the pq coordinates contains a single fixed point z_X, whose stable manifold S (thin curve) and unstable manifold $\mathcal{U}$ (thick curve) intersect to form a homoclinic tangle. The capture lobes C_n are shaded white, the escape lobes E_n purple, and the complex light blue.

shaped region bounded by the stable/unstable manifolds, all trajectories are bound forever. Outside this region, all trajectories escape, either to the southwest or the northeast in Fig. 5.

We now consider a nonzero magnetic field. Figure 6 is the surface-of-section plot for $B=4.5$, $E=-1.3$. As before, there are two unstable fixed points. However, their stable and unstable manifolds no longer coincide, but rather intersect transversely, forming a complicated pattern of curves called a heteroclinic tangle. This complicated structure produces phase-space transport and escape. In particular, each intersection between $\mathcal{L}_0$ and the stable manifold $\mathcal{S}_\ell$ or $\mathcal{S}_r$ produces a critical angle, i.e., an edge of an icicle, in Fig. 2(b). The infinity of icicles (and hence the infinity of electron pulses) thus results from the infinity of such intersections. We elaborate on this in Secs. III D and IV.

D. The homoclinic tangle

We simplify Fig. 6 by defining new canonical coordinates (q,p) that exploit the inversion symmetry $(v,p_v)\mapsto-(v,p_v)$. In terms of canonical polar coordinates $I=(p_v^2+v^2)/2$ and $\phi=-\tan^{-1}(p_v/v)$, we define $p=-\sqrt{I}\sin 2\phi=\sqrt{2}vp_v/\sqrt{v^2+p_v^2}$ and $q=\sqrt{I}\cos 2\phi=(v^2-p_v^2)/\sqrt{2(v^2+p_v^2)}$. In these new (q,p) coordinates, $+(v,p_v)$ and $-(v,p_v)$ are identified. Thus, the surface-of-section plot in these coordinates, as shown in Fig. 7, contains a single unstable fixed point z_X whose stable and unstable manifolds intersect transversely, forming a homoclinic tangle. The vertical line of initial conditions in Fig. 6 becomes a horizontal line in Fig. 7, terminating at $q=p=0$.

We now review how a homoclinic tangle, as in Fig. 7, produces phase-space transport and escape [12–16]. Since some of the structure in Fig. 7 is hard to resolve, we include a qualitative picture in Fig. 8(a). Similar qualitative tangles occur in Figs. 8(b) and 8(c) and in Fig. 3 of Ref. [15] and Figs. 3 and 4 of Ref. [16]. The point $\mathbf{P}_0$ is a transverse homoclinic intersection, i.e., an intersection between the stable ($\mathcal{S}$) and unstable ($\mathcal{U}$) manifolds. The segments of $\mathcal{S}$ and $\mathcal{U}$ joining z_X to $\mathbf{P}_0$ bound a region of the plane which we call the *complex*. Roughly speaking, points within the complex correspond to the excited neutral atom. If a trajectory maps outside the complex, it will subsequently progress to infinity, resulting in ionization. We therefore need to understand how points map out of the complex.

The homoclinic intersection $\mathbf{P}_0$ iterates forward to $\mathbf{P}_1,\mathbf{P}_2,\mathbf{P}_3,...$, converging to z_X along the upper $\mathcal{S}$ boundary of the complex. Similarly, it iterates backward to $\mathbf{P}_{-1},\mathbf{P}_{-2},\mathbf{P}_{-3},...$, converging to z_X along the lower $\mathcal{U}$ boundary of the complex. Between $\mathbf{P}_0$ and $\mathbf{P}_1$ is another homoclinic intersection $\mathbf{Q}_0$, whose iterates $\mathbf{Q}_n$ are interleaved between the $\mathbf{P}_n$. The segments of $\mathcal{S}$ and $\mathcal{U}$ that join $\mathbf{P}_0$ to $\mathbf{Q}_0$ in Figs. 7 and 8 bound a region called the escape lobe E_0. Similarly, the segments that join $\mathbf{Q}_{-1}$ to $\mathbf{P}_0$ bound the capture lobe C_0. The forward and backward iterates of these lobes produce a sequence of escape lobes E_n and of capture lobes C_n. Some of these lobes are shown in Figs. 7 and 8.

Transport in and out of the complex occurs via a "turnstile" [12]: The escape lobe E_{-1}, which is inside the complex, maps to E_0, which is outside the complex; similarly, the capture lobe C_0, which is outside the complex, maps to C_1, which is inside the complex. All points that escape in n iterates lie in the lobe E_{-n}.

We characterize the structure of the tangle by two quantities, a local geometric quantity α and a global topological quantity D. (i) The Liapunov factor $\alpha>1$ is the largest eigenvalue of the Poincaré map, linearized about the fixed point z_X. It characterizes the rate at which E_n and C_n become thinner as their bases converge upon z_X. (ii) The minimum delay time D is the fewest iterates any scattering trajectory may spend within the complex. (A scattering trajectory is one that begins outside the complex, is captured by the complex, spends some number of iterates within the complex, and eventually escapes.) Alternatively, the delay time D is the smallest n such that $E_{-(n+1)}$ intersects C_0 or, more generally, $E_{k-(n+1)}$ intersects C_k for arbitrary k. For Figs. 7 and

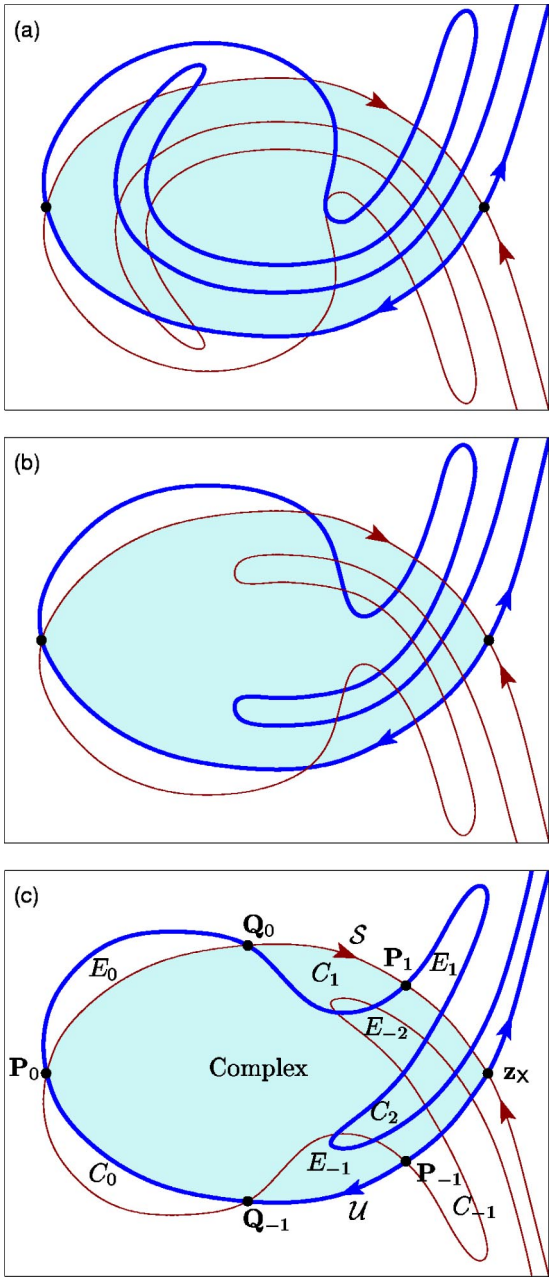

FIG. 8. Three qualitative depictions of homoclinic tangles with different topological structure: (a) $D=1$ (qualitatively the same as Fig. 7), (b) $D=2$ (E_{-2} intersects C_1 but overshoots it), (c) $D=2$. The labels in (c) apply to (a) and (b) as well. The complex is the shaded region bounded by the segments of $\mathcal{S}$ and $\mathcal{U}$ joining z_X to $\mathbf{P}_0$. The capture lobe C_1 is bounded by the segments of $\mathcal{S}$ and $\mathcal{U}$ joining $\mathbf{Q}_0$ to $\mathbf{P}_1$. Other lobes are defined similarly. The progression from (a) to (c) corresponds to fixing the scaled magnetic field B while decreasing the scaled energy E toward the saddle energy $E=-2$.

8(a), the intersection between E_{-2} and C_0 implies $D=1$. For Figs. 8(b) and 8(c), however, the intersection between E_{-2} and C_1 implies $D=2$; the lobe E_{-3} (not shown) would reach over and intersect C_0.

Figure 4(b) shows the numerically computed Liapunov exponent $\ln \alpha$ as a function of E and B. For $B \gtrsim 3$, $\ln \alpha$ is approximately (see Appendix A)

$$\ln \alpha \approx T_{\mathrm{po}} \sqrt{2} \left(1 - \frac{3}{8} \langle \rho^2 \rangle \right), \tag{15}$$

where T_{po} is given by Eq. (14) and

$$\langle \rho^2 \rangle = \frac{E+2}{B^2/4+1} \tag{16}$$

is the (approximate) average value of ρ^2 along the periodic orbit. Under this approximation, $\ln \alpha$ has a weak linear dependence on E through $\langle \rho^2 \rangle$, consistent with the data in Fig. 4(b). Furthermore, as B increases, $\ln \alpha$ converges to zero proportional to $\sqrt{2} T_{\mathrm{po}}$. For $E=-1.3$ and $B=4.5$, direct numerical computation yields $\ln \alpha = 1.743$, whereas Eq. (15) yields the good approximation $\ln \alpha = 1.726$.

The two solid curves in Fig. 4(b) denote changes in the topological parameter D. Based on numerical computations, $D=1$ in regions 1 and 1^+, $D=2$ in regions 2 and 2^+, and $D>2$ in the region to the left and below region 2. The dashed curves denote where the lobes exhibit "overshoot," a point revisited in Sec. IV C.

IV. EPISTROPHE STRUCTURES

A. Epistrophes in the discrete-escape-time plot

Figure 2(c) records the number of iterates of the Poincaré map required for a point θ along $\mathcal{L}_0$ to escape the complex, i.e., to land in the escape lobe E_0. This discrete-time plot gives a rectification of the continuous-time plot Fig. 2(b). Each icicle is straightened into a single *escape segment* with constant iterate number. Each escape segment that escapes on the nth iterate is an interval of intersection between the escape lobe E_{-n} and the line of initial conditions $\mathcal{L}_0$. For example, the intersection between E_{-2} and $\mathcal{L}_0$ in Fig. 7 yields the segment labeled A1 in Fig. 2(c).

Throughout the discrete-escape-time plot Fig. 2(c) and on all scales there are regular sequences of escape segments, which we call *epistrophes*. ("Epistrophe" is a term from rhetoric or poetry meaning "a regular, repeated ending following variable beginnings.") We previously [15] studied general properties of epistrophes arising from a general homoclinic tangle, which we summarized in an epistrophe theorem: (i) An epistrophe is an infinite sequence of successive escape segments ϵ_k, $k=k_0,\ldots,\infty$, that escape on the kth iterate. (ii) Each epistrophe converges monotonically upon the end point of an earlier escape segment. (iii) This convergence is geometric with rate equal to the Liapunov factor α of the fixed point $\mathrm{z_X}$. More precisely, let w_k be the width of segment ϵ_k, g_k be the distance between ϵ_k and ϵ_{k+1}, and d_k be the distance from ϵ_k to the point of convergence. Then,

$$\lim_{k\to\infty} w_k \alpha^k = K_w, \tag{17}$$

$$\lim_{k\to\infty} g_k \alpha^k = K_g, \tag{18}$$

$$\lim_{k\to\infty} d_k \alpha^k = K_d, \tag{19}$$

for some $K_w, K_g, K_d > 0$. (iv) The asymptotic tails of any two epistrophes differ only by a change of scale. Equivalently,

$$\lim_{k\to\infty} \frac{w_k}{g_k} = \chi, \tag{20}$$

$$\lim_{k\to\infty} \frac{w_k}{d_k} = \phi, \tag{21}$$

where $\chi, \phi > 0$ do not depend on the epistrophe considered. (v) With rare exception (not seen in the present paper), an epistrophe converges upon each end point of every escape segment.[2]

The recursive structure of the epistrophes gives the escape-time plot structure-within-structure on all scales. The removal of escape segments on each iterate is analogous to the construction of the middle-third Cantor set, and the set of trajectories that never escape has an analogous fractal structure.

The epistrophe structure of Fig. 2(c) is illustrated in Fig. 2(d). The A epistrophe (of which the first four segments A1⋯A4 are shown) converges upon the upper end point of the direct segment. Similarly, the B and C epistrophes converge upon the upper and lower end points of the A1 segment, respectively. The first segments (unlabeled) of the two epistrophes converging upon the upper and lower end points of the A2 segment occur on the fifth iterate. The escape segments in each epistrophe decay with asymptotic rate $\alpha = 5.71$.

In Ref. [16], we discussed at which iterate k_0 an epistrophe begins. The topological structure of the homoclinic tangle shows that there must be a certain "minimal set" of escape segments. We developed a symbolic algorithm for computing this minimal set and showed that the escape segments within the set eventually, i.e., at large enough iterate, obey an "epistrophe start rule": An escape segment on the nth iterate spawns two new epistrophes on iterate $k_0 = n + D + 1$. This rule is seen in Fig. 2(d), for which $D+1=2$. (Recall that $D=1$ in Fig. 7). The B and C epistrophes start at $n=4$, two iterates after the A1 segment at $n=2$. Similarly, the A2 segment ($n=3$) spawns two new epistrophes at $n=5$.

Calculations show that there are also escape segments that do not belong to the minimal set. These segments are not predicted by the symbolic algorithm mentioned above, and they do not fit the simple pattern predicted by the Epistrophe Start Rule. Such a segment, which we call a *strophe*, is marked by an asterisk in Figs. 2(b)–2(d). Numerical evidence indicates that strophes tend to be big segments and that at large iterate they are the dominant escape segments, compared to those predicted in the minimal set.

We use the term *epistrophic self-similarity* to describe the above situation: throughout the escape-time plot and on all scales there are epistrophes; they are all asymptotically self-similar and each is similar to every other. However, there may also be strophe segments which occur on all scales and which, at long times, may come to dominate the regular epistrophe structure.

[2]The exception only occurs when the end point in question is not on the stable manifold. This only happens on the $\mathcal{U}$ boundary of the complex.

B. Epistrophe structure of pulse trains

To each escape segment there corresponds an icicle, and hence an electron pulse. Thus, an epistrophe of escape segments produces an *epistrophe* of electron pulses, where the pulse sizes decay exponentially with rate α. In Figs. 2(a) and 2(b) we explicitly connect the first nine pulses to their corresponding icicles and label them according to the scheme in Fig. 2(d). The first pulse is the large direct pulse. The second, third, and sixth pulses are the first three pulses of the A epistrophe. Notice the rapid decay in pulse size, since $\alpha = 5.71$. The time between successive pulses in an epistrophe is roughly equal to the period $T_{\rm po} = 1.28$, the time for the periodic orbit in Fig. 3 to travel from $u=0$ back to $u=0$ (Sec. III B). (This result is exact for the asymptotic behavior of an epistrophe.)

The epistrophe start rule is also reflected in the pulse train. Since $D+1=2$, the two pulses B1 and C1, spawned by the A1 pulse, occur almost concurrently with the A3 pulse, or about $2T_{\rm po}$ after the A1 pulse. The B2 and C2 pulses follow roughly $T_{\rm po}$ after the B1 and C1 pulses.

The next pulse in the train is associated with the strophe segment (marked by the asterisk). Notice that it is large compared to other pulses nearby in time. This is typical of the behavior we observe for the strophe segments and their associated pulses, and numerical evidence indicates that the strophe pulses come to dominate at long times.

This completes our analysis and explanation of the unaveraged pulse train, shown as the thin line in Fig. 2(a). In Sec. V, we discuss the resolution of pulses in the energy-time-averaged pulse train, shown as the thick line. First, however, we consider how the structure of the pulse train changes when the minimum delay time D is changed.

C. Varying the topological parameter *D*

At $B=4.5$, $E=-1.92$, the minimum escape time D equals 2, as shown in Fig. 4(b). Figure 8(c) depicts the qualitative topological structure of the $D=2$ homoclinic tangle. This topological structure is reflected in the structure of the electron pulse train shown in Fig. 9. In particular, the Epistrophe Start Rule (Sec. IV A) states that epistrophes are spawned after $D+1=3$ iterates, rather than the two iterates seen in Fig. 2. For example, the B and C epistrophes in Fig. 9(d) are spawned at $n=6$, three iterates after the A1 segment. Similarly, the B1 and C1 pulses are roughly concurrent with the A4 pulse in Fig. 9(a).

The topology of the tangle in Fig. 8(b) is intermediate between Figs. 8(a) and 8(c). Passing from Fig. 8(a) to Fig. 8(b), the lobe E_{-2} contracts, so that it no longer intersects C_0. The elimination of this intersection implies $D=2$. The "tip" of E_{-2}, however, still "overshoots" its intersection with C_1. Passing from Fig. 8(b) to Fig. 8(c), E_{-2} continues to contract so that it does not overshoot C_1. Figure 4(b) provides parameter ranges for these topologies: region 2 has $D=2$ with no overshoot, region 2^+ has $D=2$ with overshoot, region 1 has $D=1$ with no overshoot, and region 1^+ has $D=1$ with overshoot.

The overshoot of the lobe in Fig. 8(b) creates additional intersections with the line of initial conditions (and conse-

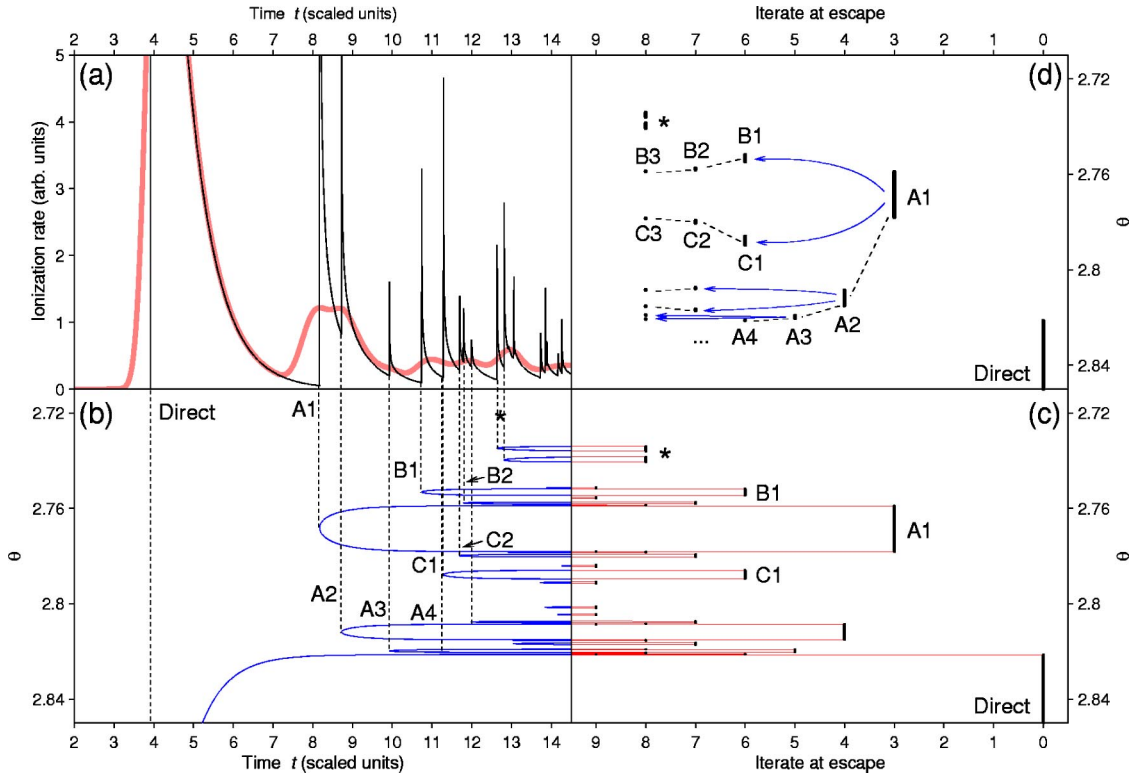

FIG. 9. A. sequence of plots analogous to Fig. 2 with $B=4.5$, $E=-1.92$. The averaged pulse train in (a) is excited to $N=80$ with $\Delta_t=0.17$, $\Delta_E=0.019$. The physical field strengths are $\hat{F}=8.5$ V/cm, $\hat{B}=0.27$ T, and one scaled unit of time equals 93 ps.

quently additional escape segments and pulses) that are not accounted for in the epistrophe start rule of Sec. IV and Ref. [16]. However, such overshoot does not produce the strophe segments (and pulses) in Figs. 2 and 9, which are created by topological structure of another variety. In a future publication we will present a more detailed topological analysis of the tangle to address these phenomena. See also Refs. [14,17].

V. PULSE RESOLUTION

We study how energy and time averaging affects the resolution of electron pulses. In Sec. V F we also consider how different initial angular distributions affect pulse strength.

A. Variation of arrival time with energy

At a fixed energy, each pulse has a sharp initial arrival time, which is the earliest time of the corresponding icicle. As the energy is varied, this arrival time also varies, as shown in Fig. 10 for the early icicles. As the energy is increased, the trajectories move faster and tend to strike the detector earlier, implying a general shift of the pulses toward earlier times.

Six of the curves in Fig. 10 are nearly straight lines, with only a slight bowing. The remaining three curves, however, are substantially bent. This bending is related to the creation of the corresponding icicles. For example, the strophe curve, denoted with an asterisk, is created at $E\approx-1.34$, where it has an infinite arrival time. This arrival time rapidly decreases as the energy is raised, until the curve enters Fig. 10 from the right. It then bends into a nearly straight vertical curve.[3] The same qualitative behavior is seen for the A1 and C1 curves. The remaining six curves bend similarly, but outside the range of the figure.

[3]Shortly above the point where the strophe curve turns vertical, it bifurcates into two curves, representing the splitting of the initial icicle into two icicles.

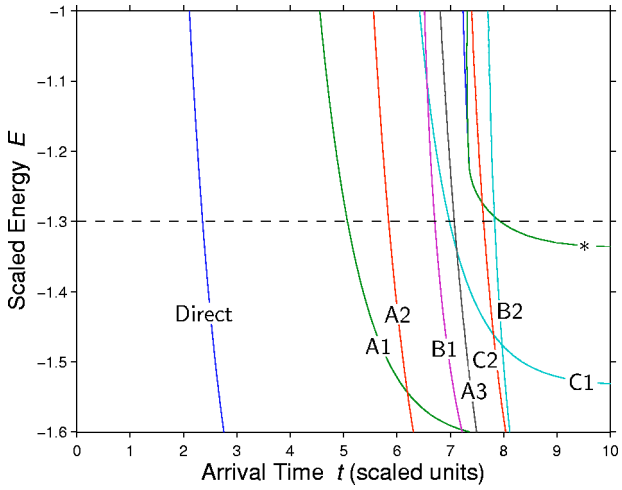

FIG. 10. The (earliest) arrival time of each icicle labeled in Fig. 1(b) is shown as a function of energy. The value $B=4.5$ is held fixed. For many icicles, the behavior is close to linear over the energy range plotted. However, A1, C1, and * display notable nonlinear behavior.

It is fortunate that the basic structure of the pulse train is roughly constant over the range of excitation energies ΔE used in averaging. This constancy is exhibited by the arrival times (Fig. 10) as well as the weak variation of $T_{\rm po}$ and α as functions of E at $B=4.5$ (Fig. 4).

B. The optimal Δ_t

We ask how the energy dependence of the curves in Fig. 10 affects the resolution of a pulse in the energy-time-averaged pulse train. If in Fig. 10 the arrival time of an icicle were independent of energy, we would get the sharpest measured electron pulse by minimizing the duration of the laser pulse. However, since the arrival time does vary with energy, we optimize the resolution of an electron pulse by balancing the energy spread and time duration of the laser pulse.

For a given electron pulse, assume that Δ_E is small enough that its curve in Fig. 10 may be approximated by a straight line. Then Δ_E creates a deviation in arrival time $\Delta_t' = |b|\Delta_E$, where $b=(dt/dE)|_{E=E_c}$ is the inverse slope of the curve in Fig. 10, at the central energy. The unaveraged pulse is thus averaged by convolving with two Gaussians of widths Δ_t and $\Delta_t'=|b|\hbar_s/(2\Delta_t)$, or equivalently, by convolving with a single Gaussian of width $\Delta_{t,\rm tot}=\sqrt{\Delta_t^2+\Delta_t'^2}$. The minimum value of $\Delta_{t,\rm tot}$ is $\sqrt{|b|\hbar_s}$ and is attained at

$$\Delta_t = \Delta_{t,\rm opt} = \sqrt{\frac{|b|\hbar_s}{2}}, \tag{22}$$

$$\Delta_E = \Delta_{E,\rm opt} = \sqrt{\frac{\hbar_s}{2|b|}}. \tag{23}$$

Unless otherwise stated, we compute $\Delta_{t,\rm opt}$ by evaluating b for the direct pulse. For $B=4.5$, $E=-1.3$ this yields $b\approx -1.00$ and $\Delta_{t,\rm opt}\approx\Delta_{E,\rm opt}$. This works well because the slopes of most other curves in Fig. 10 do not differ much from that of the direct pulse. The smoothed curves in Figs. 2(a) and 9(a) were obtained in this way.

C. Increasing the excitation energy

We imagine increasing the physical excitation energy $\hat{E}=-1/(2N^2)$ while simultaneously adjusting the physical field strengths $\hat{F}$ and $\hat{B}$ so that the scaled quantities E and B are held fixed. This leaves the classical Hamiltonian unchanged [either Eq. (1) or Eq. (13)], while decreasing the effective Planck constant $\hbar_s$ by $1/N$ [see Eq. (2)]. Thus, the extent of the Gaussian wave packet in the energy-time plane decreases by $1/N$ and the energy-time-averaged pulse train more closely approximates the unaveraged pulse train. Figure 11 shows this convergence for $N=20,80,400$, in each case choosing Δ_t according to Eq. (22). The width of the averaged electron pulses is governed by $\Delta_{t,\rm tot}$, which scales as $1/\sqrt{N}$.

D. Averaging the strophe pulse

Notice in Fig. 2(a) that the energy-time-averaged strophe pulse is not centered on the unaveraged strophe pulse. Rather it is shifted toward earlier time, preceding the B2 and C2

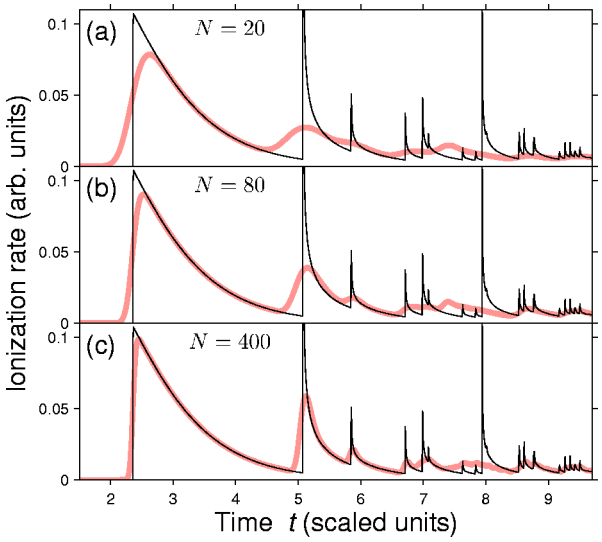

FIG. 11. The energy-time-averaged pulse train (thick curve) for $B=4.5$, $E=-1.3$ and (a) $N=20$, (b) $N=80$, (c) $N=400$. The unaveraged pulse train is the thin curve. In (a), $\Delta_t=\Delta_E=0.12$, $\hat{F}=4.8$ kV/cm, $\hat{B}=32$ T, t scale=0.81 ps; in (b), $\Delta_t=\Delta_E=0.062$, $\hat{F}=19$ V/cm, $\hat{B}=0.49$ T, t scale=52 ps; in (c), $\Delta_t=\Delta_E=0.028$, $\hat{F}=0.030$ V/cm, $\hat{B}=0.0039$ T, t scale=6.5 ns.

pulses. This phenomenon is understood by examining the strophe arrival time curve in Fig. 10. At the central energy $E_c=-1.3$ (the dashed line), the curvature is significant and affects the energy averaging as follows. A Gaussian distribution of energies about E_c places equal weight above the dashed line as below. However, the variation in arrival time above the line is smaller than the variation below the line, since the curve becomes more vertical above E_c. Therefore, the energy-averaged pulse density tends to pile up at a time preceding the unaveraged pulse. As Δ_E increases, this shift becomes more pronounced, as illustrated in Fig. 12. For large enough Δ_E ($\Delta_E\gtrsim 0.04$), this shift is further enhanced by the fact that the strophe pulse disappears entirely below $E\approx -1.34$. The shift is also enhanced by an increase in the strength of the pulse (i.e., the width of the escape segment) as the energy increases.

Finally, the temporal shift discussed here occurs for any pulse whose arrival time exhibits large curvature, i.e., the "strophe" nature of the pulse is not relevant.

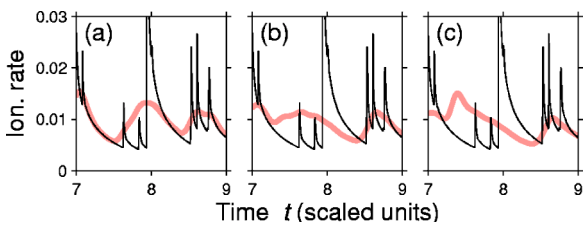

FIG. 12. For $B=4.5$, $E=-1.3$, and $\Delta_t=0.062$, the energy-time-averaged strophe pulse (located at $t\approx 8$) is seen to shift to earlier times as Δ_E increases: (a) $\Delta_E=0.013$ ($N=400$), (b) $\Delta_E=0.038$ ($N=133$), (c) $\Delta_E=0.063$ ($N=80$).

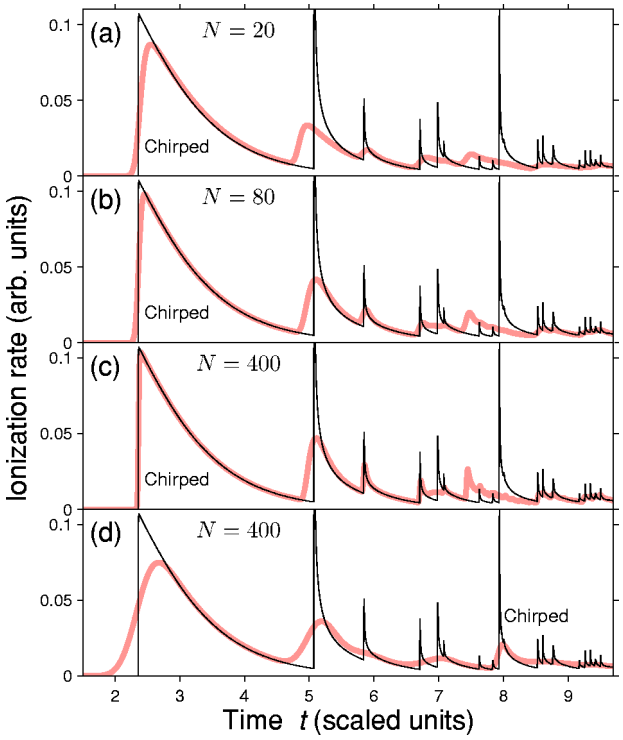

FIG. 13. The energy-time-averaged pulse train (thick curve) generated by a chirped laser pulse for $B=4.5, E=-1.3$. The chirping for plots (a)–(c) is calibrated on the direct pulse with (a) $N=20$, $\Delta_t=0.06$, $\Delta_E=0.26$; (b) $N=80$, $\Delta_t=0.04$, $\Delta_E=0.097$; (c) $N=400$, $\Delta_t=0.01$, $\Delta_E=0.078$. The chirping for plot (d) is calibrated on the strophe pulse with $N=400$, $\Delta_t=0.05$, $\Delta_E=0.016$.

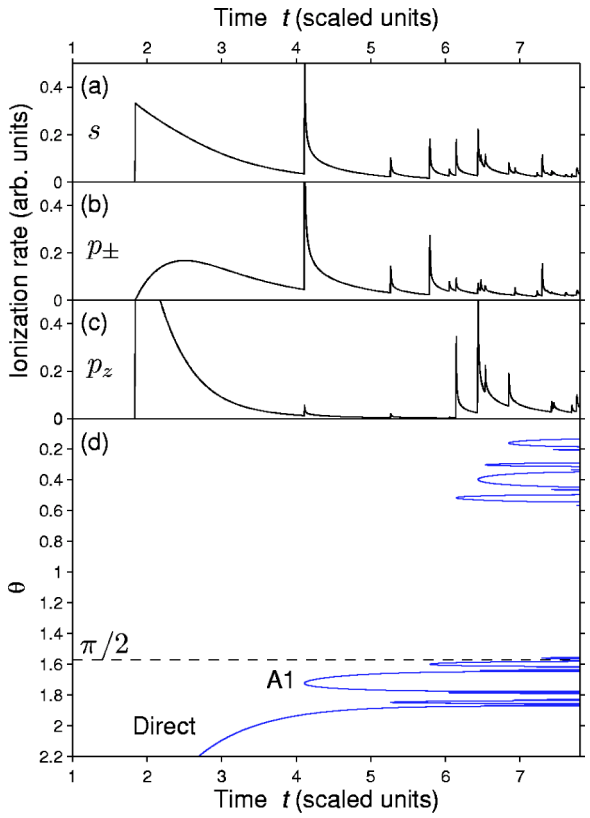

FIG. 14. The unaveraged pulse train at $B=4.5$, $E=-0.50$ for three different initial angular distributions: (a) s, (b) $p_\pm$, (c) p_z. Part (d) shows the corresponding escape-time plot.

E. Chirping

Chirping the laser pulse can increase the time resolution of a pulse within the train. Since higher-energy electrons reach the detector earlier than lower-energy ones, we can enhance the resolution by chirping the laser pulse so that higher-energy electrons begin later than lower-energy ones. We increase the frequency of the chirped pulse linearly in time with rate $1/b=(dE/dt)|_{E=E_c}$, matching the linear dependence of arrival time on energy for a given pulse (see Sec. V B). More precisely, the Wigner function of the linearly chirped Gaussian pulse is

$$W(E,t)=Ae^{-(t-bE)^2/(2\Delta_t^2)}e^{-(E-E_c)^2/(2\Delta_E^2)}. \tag{24}$$

We determine Δ_t by numerically adjusting it until a good resolution is obtained.

Figure 13 shows energy-time-averaged pulse trains generated by a chirped laser pulse. In parts (a)–(c), the chirping rate $1/b$ matches the direct pulse. Hence, the direct pulse shows a notable enhancement over Fig. 11 for all three values of N. Other pulses whose slopes in Fig. 10 roughly match that of the direct pulse are also enhanced, whereas those pulses whose slopes differ markedly from the direct pulse have weaker, if any, enhancement. This distinction is clearly seen in pulses four and five. In Fig. 10, the slope of the direct pulse closely matches that of pulse four (B1), but not that of pulse five (C1). Consequently, in Figs. 13(a)–13(c) pulse four is sharp (especially for $N=400$) whereas pulse five is broad and not readily discernible.

As explained in Sec. V D, the strophe pulse in Figs. 13(a)–13(c) is shifted to earlier time when averaged. The resolution of the strophe pulse is also increased when compared to Fig. 11. This is because the slope of the strophe curve in Fig. 10 is close to that of the direct pulse above $E_c=-1.3$.

Figure 13(d) shows the pulse train generated by a chirp calibrated on the strophe pulse, rather than the direct pulse. The resulting strophe pulse is close to its unaveraged position and width. Since the chirp is not matched to the other pulses, they are significantly wider than in Fig. 13(c).

F. Varying the angular distribution

In Fig. 2(a), the initial outgoing angular distribution is an s wave. Any other distribution $|\mathcal{Y}(\theta)|^2$ (such as a p wave) does not change the overall character of our results. However, the size of an electron pulse will change, depending on the angle at which it is launched, i.e., on the θ position of the corresponding icicle. This effect is most dramatic for icicles near a zero of the angular distribution, which produce highly suppressed pulses, as demonstrated in Fig. 14. The scaled energy $E=-0.5$ is chosen so that the cluster of icicles near A1 will be near $\theta=\pi/2$. Another cluster of icicles is near $\theta=0$. For an initial s state [Fig. 2(a)], $|\mathcal{Y}(\theta)|^2=1$ is uniform.

For an initial $p_\pm$ state [Fig. 2(b)], however, there is a node at $\theta=\pi$, which suppresses the direct pulse, and a node at $\theta=0$, which suppresses the upper icicle cluster.[4] Conversely, for an initial p_z state [Fig. 2(c)], there is a node at $\theta=\pi/2$, which suppresses the A1 icicle cluster. Thus, for a p_z-state the pulse train exhibits a prominent direct pulse followed by a lull, due to the suppressed A1 cluster, and the subsequent arrival of the $\theta=0$ cluster of pulses.

VI. CONCLUSIONS

We predict that an excited hydrogen atom in applied fields can decay through emission of a train of electron pulses. Our analysis models the initial outgoing electron wave function by an ensemble of classical trajectories, a portion of which eventually strike the detector. For the pulsed laser experiment under consideration here, quantum interference should not play a major role at the early times studied, since the electron pulses do not significantly overlap one another at the plane of the detector. However, for a continuous-wave excitation of an atom, ionizing electron trajectories will create an interference pattern on the detector. In a remarkable series of experiments, such patterns have been imaged for both photodetachment [18] and photoionization [19] in an applied electric field. In future work, we will apply the theoretical tools used here to study such interference patterns for continuous-wave photoionization of hydrogen in external electric and magnetic fields.

Finally, the existence of pulse trains is a direct consequence of chaotic escape arising from a homoclinic tangle. As such, pulse trains should be visible in other systems displaying this escape mechanism, for example certain open billiard geometries. Such geometries can be physically realized as light or microwave cavities. Pulsed microwave experiments thus give another potential route to measuring chaos-induced pulse trains.

APPENDIX A: PERTURBATIVE ANALYSIS ABOUT THE PERIODIC ORBIT

We develop approximations for both $T_{\rm po}$ and $\ln\alpha$. For sufficiently large B, the radius of the periodic orbit in ρz space is small enough to justify expanding the potential Eq. (1b) through second order in ρ,

$$V(\rho,z)=\frac{1}{8}B^2\rho^2+\frac{1}{2}\frac{\rho^2}{|z|^3}-\frac{1}{|z|}+z+O(\rho^4). \tag{A1}$$

The z position of the periodic orbit lies near the classical saddle $z=-1$, where the external electric field is balanced by the Coulomb field. Using the approximation $z=-1$, the ρ behavior is to lowest order harmonic, with angular frequency $\sqrt{B^2/4+1}$. Note that this frequency assumes ρ makes a full oscillation through both positive and negative values. Restricting ρ to the physically allowed positive values yields Eq. (14). This approximation gives a relative error of 3% or better for $B\gtrsim 2$.

We develop an approximation for $\ln\alpha$ by considering the z dependence of Eq. (A1). Near the approximate position $z=-1$ of the periodic orbit, the ρ motion is much faster than the z motion, producing an effective ρ-averaged z potential,

$$V_z(z)=\frac{1}{2}\frac{\langle\rho^2\rangle}{|z|^3}-\frac{1}{|z|}+z, \tag{A2}$$

where $\langle\rho^2\rangle$, given by Eq. (16), is ρ^2 averaged over one ρ oscillation, within the harmonic approximation. The unstable critical point of V_z occurs at $z_c=-1+3\langle\rho^2\rangle/4$ with curvature $|d^2V_z(z_c)/dz^2|=2-3\langle\rho^2\rangle/2$. The Liapunov exponent is then approximately

$$\ln\alpha\approx T_{\rm po}\sqrt{|d^2V_z(z_c)/dz^2|}\approx T_{\rm po}\sqrt{2}\left(1-\frac{3}{8}\langle\rho^2\rangle\right). \tag{A3}$$

This approximation gives a relative error of 10% or less for $B\gtrsim 3$.

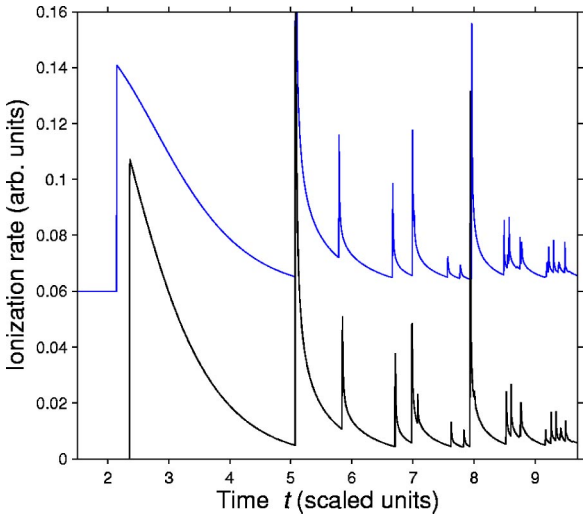

FIG. 15. Two unaveraged pulse trains for $B=4.5$, $E=-1.3$. For the lower train, the detector is placed at $z=-4$. For the upper train (vertically offset by 0.06), the detector is placed at $z=-1.2\times10^4$. The upper train is shifted in time to align its second pulse with that of the lower train.

APPENDIX B: DEPENDENCE OF PULSE TRAINS ON THE DETECTOR POSITION

The continuous-escape-time plots and ionization rates in this paper were computed for a detector at $z=-4$, which is unrealistically close to the atom by several orders of magnitude. In this appendix, we consider placing the detector farther away. We find that the effect on the pulse train is minimal.

The position z_d of the detector in scaled units is related to its position $\hat{z}_d$ in physical (atomic) units by $z_d=\hat{z}_d\hat{F}^{1/2}=\hat{z}_d\hat{E}/E=\hat{z}_d/(2N^2|E|)$. For $N=80$, $E=-1.3$, and $\hat{z}_d=-2\times10^8\approx-1$ cm, the scaled position of the detector is $z_d=-1.2\times10^4$.

[4]To be precise, for a $p_\pm$-state $\mathcal{Y}(\theta,\phi)$ is not constant in ϕ, but $|\mathcal{Y}(\theta,\phi)|^2$ is. Furthermore, the classical Hamiltonians (1) or (13) are applicable even with a few quanta in L_z, because the L_z contributions to the Hamiltonians occur at order $\hbar_s^2$.

We integrate trajectories up to a "virtual" detector at $z_d' = -4$. Below $z = z_d'$ it is reasonable to ignore the Coulomb force, and the dynamics separates into uniform acceleration $a_z = -1$ in the z direction and cyclotron motion in the transverse direction. Under uniform acceleration, the time δt for a trajectory to travel between the virtual detector at z_d' to the physical detector at z_d is

$$\delta t = p_z + \sqrt{p_z^2 + 2|z_d - z_d'|} \approx p_z + \sqrt{2|z_d|}, \qquad \text{(B1)}$$

where $p_z < 0$ is the z momentum at the virtual detector. The approximation in Eq. (B1) holds because $|z_d'| \ll |z_d|$ and because the maximum value of p_z^2 is $2(E - z_d') < 2|z_d'|$.

The second term in Eq. (B1), though large, is independent of trajectory and only shifts the pulse train in time. The first term in Eq. (B1), however, varies with trajectory, but only by a small amount. Figure 15 shows the unaveraged pulse train with and without the correction (B1). (The origin has been shifted in time to make the second pulses coincide.) We do see slight shifts in the relative arrival times of pulses with and without this term, but not by substantial amounts. These slight shifts would decrease even further if the virtual detector were moved lower. Finally, Eq. (B1) shows there is no significant change in the relative arrival times due to varying the position of the physical detector.

[1] G. M. Lankhuijzen and L. D. Noordam, Phys. Rev. Lett. **76**, 1784 (1996); Opt. Commun. **129**, 361 (1996).

[2] F. Robicheaux and J. Shaw, Phys. Rev. Lett. **77**, 4154 (1996); Phys. Rev. A **56**, 278 (1997).

[3] K. A. Mitchell, J. P. Handley, B. Tighe, A. Flower, and J. B. Delos, Phys. Rev. Lett. **92**, 073001 (2004).

[4] See, for example, E. Flöthmann, dissertation, Universität Bielefeld, 1994, Figs. 1.3 and 1.4; R. Ubert, dissertation, Universität Bielefeld, 1995, Figs. 2.11 and 2.12; D. M. Wang, Ph.D. thesis, College of William and Mary, Williamsburg, VA 2000, Figs. 4.5 and 4.8.

[5] (a) J. Gao, J. B. Delos, and M. Baruch, Phys. Rev. A **46**, 1449 (1992); (b) J. Gao and J. B. Delos, *ibid.* **46**, 1455 (1992); (c) J. Gao and J. B. Delos, *ibid.* **49**, 869 (1994).

[6] M. R. Haggerty and J. B. Delos, Phys. Rev. A **61**, 053406 (2000).

[7] M. L. Du and J. B. Delos, Phys. Rev. A **38**, 1896 (1988); **38**, 1913 (1988).

[8] J.-M. Mao, K. A. Rapelje, S. J. Blodgett-Ford, J. B. Delos, A. König, and H. Rinneberg, Phys. Rev. A **48**, 2117 (1993).

[9] Fractal escape-time plots and related functions are standard tools in chaotic scattering theory. In addition to Refs. [10,17] , see D. W. Noid, S. K. Gray, and S. A. Rice, J. Chem. Phys. **84**, 2649 (1986); J.-M. Petit and M. Henon, Icarus **66**, 536 (1986); B. Eckhardt and C. Jung, J. Phys. A **19**, L829 (1986); B. Eckhardt, *ibid.* **20**, 5971 (1987); C. Jung and H. J. Scholz, *ibid.* **20**, 3607 (1987); P. Gaspard and S. Rice, J. Chem. Phys. **90**, 2225 (1989); P. Gaspard, *Chaos, Scattering and Statistical Mechanics* (Cambridge University Press, Cambridge, 1998).

[10] L. Gottdiener, Mol. Phys. **29**, 1585 (1975); A. Tiyapan and C. Jaffé, J. Chem. Phys. **99**, 2765 (1993); **101**, 10 393 (1994); **103**, 5499 (1995).

[11] E. Pollak, in *Theory of Chemical Reaction Dynamics*, edited by M. Baer (CRC Press, Boca Raton, 1985), Vol. 3, p. 123.

[12] R. S. MacKay, J. D. Meiss, and I. C. Percival, Physica D **13**, 55 (1984); S. Wiggins, *Chaotic Transport in Dynamical Systems* (Springer-Verlag, New York, 1992).

[13] M. J. Davis and S. K. Gray, J. Chem. Phys. **84**, 5389 (1986); M. J. Davis, *ibid.* **83**, 1016 (1985).

[14] V. Rom-Kedar, Physica D **43**, 229 (1990); Nonlinearity **7**, 441 (1994).

[15] K. A. Mitchell, J. P. Handley, B. Tighe, S. K. Knudson, and J. B. Delos, Chaos **13**, 880 (2003).

[16] K. A. Mitchell, J. P. Handley, S . K. Knudson, and J. B. Delos, Chaos **13**, 892 (2003).

[17] B. Rückerl and C. Jung, J. Phys. A **27**, 55 (1994); C. Jung, C. Lipp, and T. H. Seligman, Ann. Phys. **275**, 151 (1999).

[18] C. Blondel, C. Delsart, and F. Dulieu, Phys. Rev. Lett. **77**, 3755 (1996); C. Blondel, C. Delsart, F. Dulieu, and C. Valli, Eur. Phys. J. D **5**, 207 (1999); C. Valli, C. Blondel, and C. Delsart, Phys. Rev. A **59**, 3809 (1999); C. Blondel, C. Delsart, C. Valli, S. Yiou, M. R. Godefroid, and S. Van Eck, *ibid.* **64**, 052504 (2001).

[19] C. Nicole, I. Sluimer, F. Rosca-Pruna, M. Warntjes, M. Vrakking, C. Bordas, F. Texier, and F. Robicheaux, Phys. Rev. Lett. **85**, 4024 (2000); C. Nicole, H. L. Offerhaus, M. J. J. Vrakking, F. Lépine, and Ch. Bordas, *ibid.* **88**, 133001 (2002).